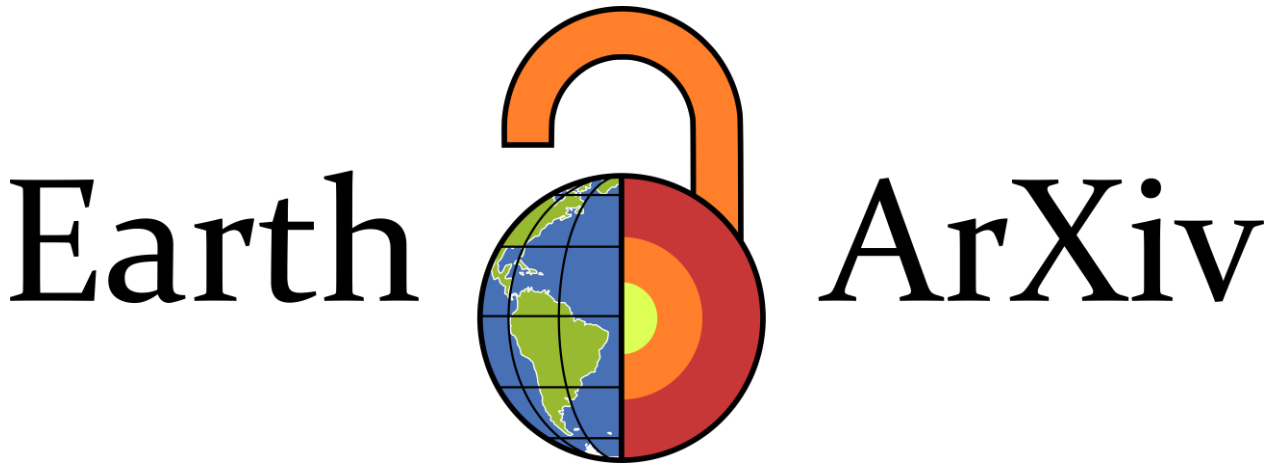


This is a non-peer-reviewed preprint submitted to EarthArXiv.

Please note the manuscript has yet to be formally accepted for publication. Subsequent versions of this manuscript may have slightly different content. If accepted, the final version of this manuscript will be available via the 'Peer-reviewed Publication DOI' link on the right-hand side of this webpage. Please feel free to contact any of the authors; we welcome feedback.

Title:

Imbibition in 3D porous media is shaped by long-range capillary- and shear-driven flow-field dynamics

Authors:

Sharon Ellman[a,b], Robert van der Merwe[a,b], Sojwal Manoorkar[a,b], Stefanie Van Offenwert[c], Wannes Goethals[a,b], Christian M. Schlepütz[d], Laurenz Schröer[a,b], Tom Bultreys[a,b]

[a]Department of Geology, PProGRess, Ghent University, Ghent, Belgium; [b]Centre for X-ray Tomography (UGCT), Ghent University, Ghent, Belgium; [c]Fluxys, Belgium; [d]Swiss Light Source, Paul Scherrer Institute, Villigen PSI 5232, Switzerland

Corresponding author: Sharon.ellman@ugent.be (S. Ellman)

Imbibition in 3D porous media is shaped by long-range capillary- and shear-driven flow-field dynamics

Sharon Ellman[a,b], Robert van der Merwe[a,b], Sojwal Manoorkar[a,b], Stefanie Van Offenwert[c], Wannes Goethals[a,b], Christian M. Schlepütz[d], Laurenz Schröer[a,b], Tom Bultreys[a,b]

[a]Department of Geology, PProGRess, Ghent University, Ghent, Belgium; [b]Centre for X-ray Tomography (UGCT), Ghent University, Ghent, Belgium; [c]Fluxys, Belgium; [d]Swiss Light Source, Paul Scherrer Institute, Villigen PSI 5232, Switzerland

Corresponding author: Sharon.ellman@ugent.be (S. Ellman)

Significance statement

When water seeps into rocks or soils, it displaces other fluids, breaking them into small fluid blobs that can be mobile or trapped. This process controls CO_2 trapping during underground sequestration, hydrogen recovery from seasonal storage, and pollutant removal from soils. Three-dimensional flows inside the blobs control their behaviour but are difficult to measure and thus poorly understood. Using synchrotron imaging, we find that when surface tension dominates, rearrangements in single pores disturb the flow far beyond them. With stronger fluid friction, the surrounding water drives recirculation cells inside trapped blobs and stretches the fluid in moving ones. This differs from simpler flows observed in 2D models and affects remobilisation of trapped fluids and mixing of dissolved substances within them.

Abstract

As a wetting fluid invades a porous material, it displaces a less-wetting fluid through sudden pore-scale events, commonly breaking the latter into isolated ganglia that can be trapped, mobilised and fragmented. Three-dimensional flows inside the ganglia shape the displacement dynamics but are difficult to measure and thus currently poorly characterised. Here, 3D X-ray particle tracking velocimetry reveals how flow inside the nonwetting phase evolves during unsteady imbibition. In the capillary-dominated regime, snap-off and cooperative pore filling disturb the flow over more than ten pore diameters for several seconds, revealing nonlocal dynamic effects in imbibition comparable to those triggered by Haines jumps in drainage. For increased viscous forces, we observe continuous fragmentation of ganglia throughout the pore space, rather than the compact front displacement predicted by phase diagrams derived from 2D micromodels. In this regime, momentum transmitted across fluid menisci drives shear near the interface and recirculation within trapped ganglia. Where previous studies describe rotational flow around a single centre in such cases, our results show that a 3D ganglion can contain a localised recirculation zone that is part of a more

complex recirculation pattern. When ganglia are mobilised, this pattern is temporarily replaced by elongational flow, which may hinder the mobilisation of non-Newtonian fluids and enhance internal mixing. The flow patterns inside the nonwetting phase during imbibition thus change with the displacement regime, the ganglion's dynamic state and with dimensionality. This affects fluid displacement, trapping and mixing in applications such as subsurface CO_2 and hydrogen storage and groundwater remediation.

1. Introduction

Multiphase flow through porous media is key to a wide range of geo-engineering and environmental processes, including subsurface CO_2 sequestration (Krevor et al., 2015) , contaminant transport in groundwater (Pak et al., 2020), subsurface energy storage (Ma et al., 2018), and water infiltration into soil. At the continuum scale, multiphase flow is commonly described using the extended two-phase Darcy formalism, which lumps capillary effects into the relative permeability term and neglects momentum transfer across fluid-fluid interfaces (Rücker et al., 2015; Solazzi et al., 2023). The validity of these assumptions depends critically on the pore-scale mechanisms governing displacements, which has been shown to vary across a range of multiphase flow regimes (F. Guo & Aryana, 2019; R Lenormand et al., 1988; Liu et al., 2015; Zhang et al., 2011). These regimes depend on the balance of capillary, viscous and inertial forces, which determines whether flow can be described as e.g. capillary fingering, stable displacement or viscous fingering (R Lenormand et al., 1988).

Significant work has been devoted to characterising the pore scale mechanisms of imbibition, the process where a nonwetting fluid is displaced by a wetting fluid in the pores. The pioneering micromodel experiments of Lenormand and coworkers established the key pore filling scenarios, including cooperative pore filling (CPF), snap-off and piston-like displacements, which govern imbibition in the capillary fingering regime (R Lenormand et al., 1988; Roland Lenormand & Zarcone, 1984). Synchrotron-based micro-CT experiments have subsequently extended this understanding to 3D, enabling detailed tracking of menisci and pore-scale fluid distributions over time during imbibition (Steffen Schlüter et al., 2017; Singh et al., 2017, 2022). While the capillary number (Ca) is typically used to characterise which force is dominant during imbibition (and drainage), it has been shown that this approach fails to fully capture the force balance (Armstrong et al., 2014). This has largely been attributed to the differing scales across which capillary and viscous forces act (Armstrong et al., 2014; H. Guo et al., 2022). However, the effects of this discrepancy appear to be secondary when flow is deep within the capillary fingering regime, meaning viscous forces are typically ignored when considering flows in this regime. As the contribution of viscous forces increases, imbibition transitions to stable displacement and eventually viscous fingering regimes. Viscous effects complicate the flow dynamics, causing phenomena such as viscous coupling (Avraam & Payatakes, 1995b), remobilisation (Datta, Ramakrishnan, et al., 2014), ganglion dynamics

(Armstrong et al., 2016; Datta, Dupin, et al., 2014; Rücker et al., 2015) and intermittency (Gao et al., 2017; Spurin et al., 2019b, 2019a). These dynamics are highly sensitive to the detailed pore geometry (Singh et al., 2022), e.g. due to the importance of wetting film flow along pore surfaces (Zhao et al., 2019). Therefore, the underlying mechanisms at play in complex 3D pore spaces are still poorly understood, meaning the reasons behind transitions from one flow regime to another in such pore spaces remain unclear. The use of 3D imaging methods, chiefly X-ray micro-computed tomography, to investigate these mechanisms has been limited due to the fast nature of these dynamics and the need to directly measure pore-scale flow fields to quantify viscous effects. For simplified 2D geometries, micromodel experiments investigating interfacial viscous coupling effects have demonstrated significant recirculating flows in trapped ganglia (Mansouri-Boroujeni et al., 2023; Roman et al., 2020). Remobilisation and ganglion dynamics micromodel studies have revealed shear-induced circulating flows (Sharma et al., 2022) as well as vortex formation (Zarikos et al., 2018) within trapped ganglia. The observation of these phenomena in micromodels suggests that complex microscopic flow field dynamics may impact imbibition in 3D pore geometries.

To fill this gap, 3D velocimetry measurements across flow regimes are necessary. Whilst synchrotron micro-CT has enabled the detailed characterisation of menisci movements over time, allowing, for example, local curvature and capillary pressure analyses (S Schlüter et al., 2016; Singh et al., 2017, 2022), the flow fields associated with these movements have typically remained unmeasured. These measurements have only recently become possible by using synchrotron X-ray Particle Tracking Velocimetry (X-ray PTV), a novel 3D PTV method using time-resolved X-ray micro-CT and fluids seeded with X-ray attenuating tracers (Bultreys et al., 2022, 2024). Bultreys et al. (2024) used this method to track the flow fields during Haines jumps, revealing surprisingly long-ranged perturbations to the velocity field. As opposed to only tracking fluid menisci over time, this method also allows for the direct measurement of 3D flow fields with a time resolution down to ~190 ms.

In this work, we investigate the underlying mechanisms when capillary and viscous forces compete. To this end, we start by directly measuring the 3D flow fields during capillary-dominated imbibition. We investigate how capillary pore filling mechanisms affect local flow fields, which potentially influence neighbouring fluid displacements. Next, we measure 3D flow fields when viscous force contributions are increased, revealing the emergence of recirculating and shear flows. This allows us to investigate the link between the flow fields and displacements in the transition-zone regime. Our results reveal that imbibition dynamics differ fundamentally across flow regimes, with direct implications for the representative elementary volume (REV) of multiphase flow, the upscaling of pore scale phenomena, the modelling of relative permeability and solute transport.

2. Results

We performed three imbibition experiments in sintered porous glass samples with different capillary numbers and viscosity ratios, spanning the capillary fingering regime, the transition zone and near-stable displacement (Figure 1). The nonwetting phase (silicone oil) was seeded with density-matched, X-ray-attenuating tracer particles (Ø10 µm). Imbibition was initiated by either retracting the nonwetting phase from the bottom of the sample, enabling the wetting phase (water or glycerol-water mixture doped with KI for image contrast) to enter from the top (Table 1), or by injecting wetting phase from the bottom. This process was imaged continuously with fast synchrotron micro-CT at 0.19 to 0.38 s per tomogram and a voxel size of 2.75 µm for a duration of 24 to 75 seconds. Tracking the tracer particles in the nonwetting phase through the 4D image series yielded Lagrangian velocity measurements. Segmentation of the fluid phases enabled individual ganglia to be tracked through mobilisation, splitting and coalescence. The detailed experimental setup and procedures are discussed in Section 4.

Combining the time-resolved velocity and fluid distribution data proves that the internal flow dynamics within the nonwetting phase differ fundamentally across imbibition flow regimes (Figure 1). We first qualitatively discuss this observation (Section 2.1), and then quantitatively characterise the flow patterns in the capillary fingering and the transition/near-stable regimes (Section 2.2 and 2.3).

2.1. Nonwetting-phase flow patterns shift from capillary fluctuations to shear flows transmitted across fluid menisci

The capillary fingering regime experiment shows a strongly fluctuating nonwetting phase flow field, spiking in response to fluid redistribution events such as snap-off, piston-like displacement or cooperative pore filling. Locally, these fluctuating flows appear to be parallel to the surface normal of the moving menisci, reflecting fluid redistribution during and immediately after the event (Figure 1 – 1, V1 and V2). In contrast, both the transition-zone and the near-stable displacement experiments exhibit longer-lived internal shear flows, which are largely parallel to the menisci (Figure 1 – 2, Figure 1 – 3, V3). These differences are consistent with the stronger momentum coupling across fluid menisci when the fluid viscosities are nearly matched (viscosity ratio $M \approx 0.9$), compared to the capillary fingering experiment. In the latter, the large viscosity difference between the fluids ($M = 0.005$) reduces the effectiveness of interfacial drag (Avraam & Payatakes, 1995a; Suwandi et al., 2022). Furthermore, there is an increasing importance of viscous forces rather than capillary effects, due to the higher Ca in this experiment.

Figure 1 – 3 and Figure S1 highlight vortex-like flow paths driven by interfacial shear in one ganglion of the near-stable displacement experiment, observed here for the first time in a 3D porous medium. The observed vortex in this case is highly localise and much smaller than the ganglion itself, forming part of a larger, complex recirculation pattern (discussed further in Section 2.3). This is in contrast with 2D micromodel

experiments, where ganglia-spanning vortices are abundant (Roman et al., 2020; Sharma et al., 2022; Zarikos et al., 2018). The difference is likely due to the more complex ramified ganglia geometries in 3D versus in 2D micromodels, where they often resemble nearly circular blobs. This may reduce the directional coherence of the interfacial drag, producing complex recirculation patterns that extend throughout ganglia, rather than ganglion-spanning vortices with near-circular flow lines. The occurrence of a ganglia-spanning vortex in a smaller, less-ramified, nearly circular ganglion in the same experiment (Figure S3) supports this. A vortex was also observed in the transition-zone experiment, which is characterised by large, immobile ganglia (Figure 1-2).

The observed flow patterns have implications for how energy is (re)distributed within the pore space during meniscus displacements. All of these phenomena may affect the local balance of forces, thereby potentially impacting consecutive meniscus movements. In the capillary fingering regime, imbibition events generate long-ranged velocity perturbations that propagate through the nonwetting phase, which will be analysed in Section 2.2. In the near-stable displacement regime, recirculating and shear flows within trapped ganglia are directly linked to the dynamics of ganglion remobilisation, as will be explored in Section 2.3.

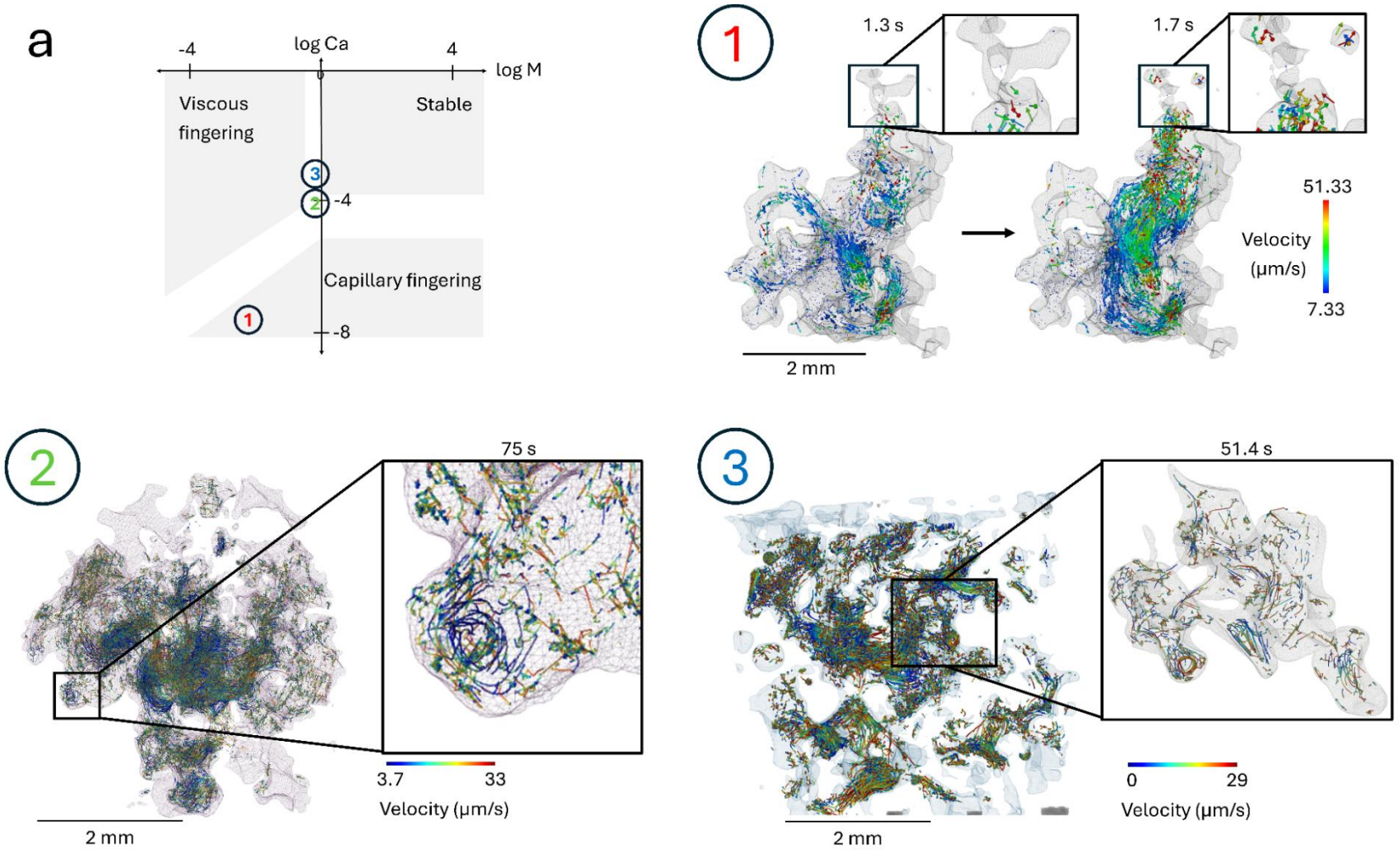


Figure 1: a) phase diagram showing where our experiments fit within the conventional flow regimes (adapted from Primkulov et al. (2021)). 1-3) visualisations of experiments, showing menisci and particle movements. 1) Imbibition in the capillary fingering regime, showing the meniscus and particle movements just prior to and then just after a snap-off. As the snap-off occurs, the particle velocities increase dramatically. 2) Imbibition in the transition-zone regime. The zoom in window shows recirculating flow. 3) Imbibition in the near-stable displacement regime. The zoom in window shows recirculating and shear flows within a trapped ganglion. While 2) and 3) exhibit shear and recirculating flows, 1) exhibits flow primarily parallel to the surface normal of moving menisci. The flow direction is from the top to the bottom of the figures. The nonwetting phase surfaces are shown as meshes while the wetting phase and grains are left transparent.

2.2. Capillary-driven flow-field fluctuations from snap-off and pore filling are non-local in space and extended in time

During imbibition in the capillary fingering regime, snap-off events occur when wetting fluid films swell and touch, leading to local meniscus instability. These events are known to significantly affect the nonwetting phase connectivity and enhance trapping (Rücker et al., 2015; Ruspini et al., 2017; Singh et al., 2017, 2022). Our experiments show that snap-offs also strongly affect the internal velocity field within the nonwetting phase (Figure 2). The observed long-ranged influence on the velocity field is surprising, as snap-offs displace small fluid volumes. The velocity perturbation reflects a sudden drop in the local capillary pressure when the snap-off takes place (Singh et al., 2017), causing the nonwetting phase to flow away from the area (Singh et al., 2017). Figure 2 shows that particle velocities throughout the entire field of view become elevated and follow tortuous pathways through the pore space, despite minimal changes to the menisci (highlighted by the yellow circle in Figure 2b, 1-3). This produces a distinct peak in the mean particle velocity across the field of view (Figure 2a).

Similar behaviour is observed during cooperative pore filling (CPF), a meniscus displacement involving the invasion of a pore by wetting phase through two or more of its neighbouring throats. During and after this event, velocities throughout the field of view become elevated and follow tortuous pathways similar to those during snap-off (Figure 2b, 4-6). The onset of the mean velocity peak associated with CPF is comparable to that of snap-off, but the velocities diminish over a longer period: approximately 1.3 s for CPF compared to approximately 0.75 s for snap-off. This is consistent with the CPF occurring over approximately eleven timesteps compared to two for the snap-off. The CPF dynamics are more akin to those of a drainage Haines jump, which also shows a rapid onset followed by a slower decay (Bultreys et al., 2024).

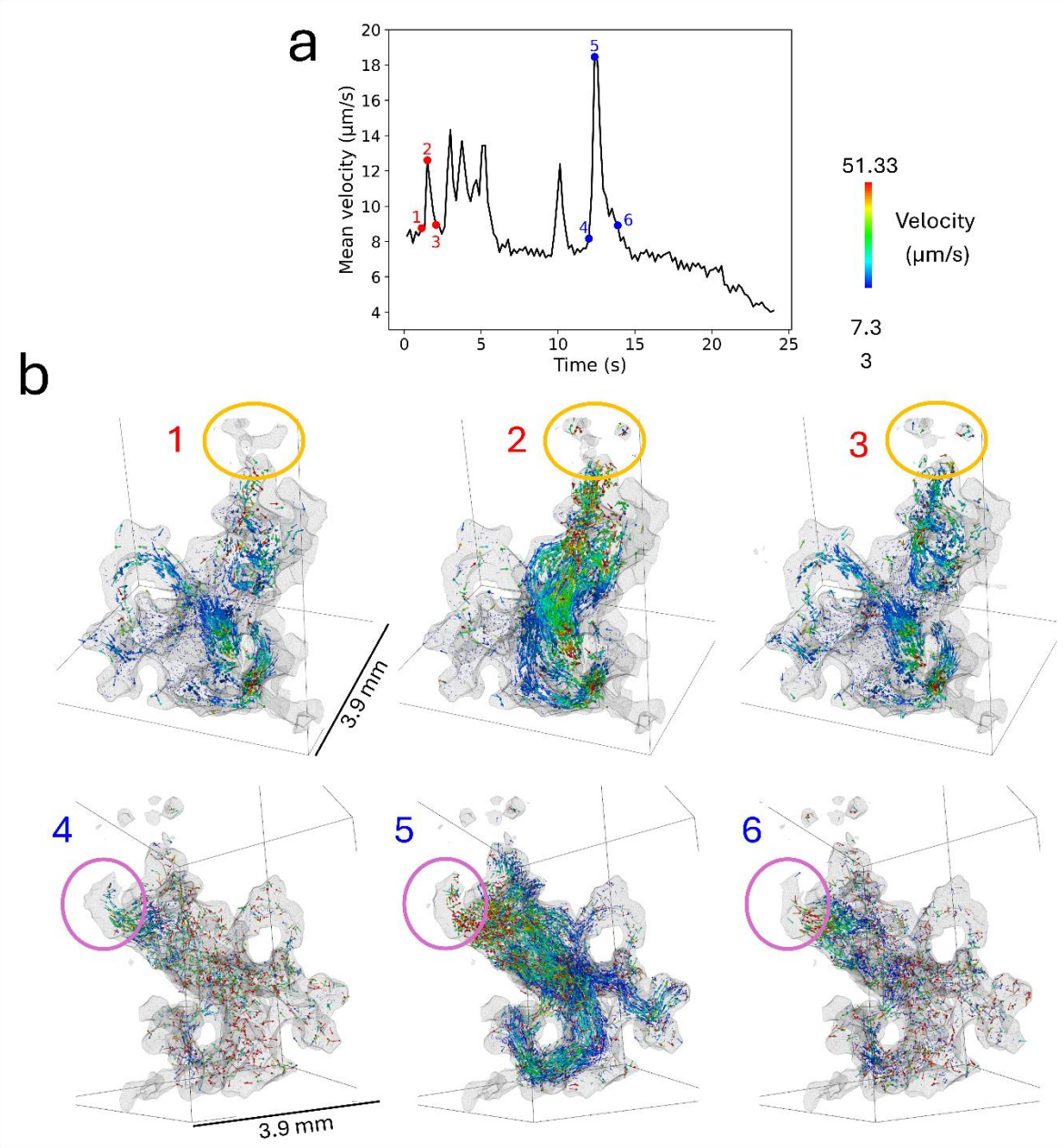


Figure 2: a) mean particle velocities during capillary-dominated imbibition; b) visualisations of a snap-off and a CPF. The nonwetting phase surface is in grey and the particles are coloured based on velocity magnitude and are scaled in size based on velocity magnitude. 1-3) Visualisation of a snap-off over three different points in time (yellow circle). 4-6) Visualisation of a CPF over three different points in time (pink circle). As both displacements occur, the velocities within the pore space spike in magnitude and the flows follow tortuous pathways. The flow direction is from the top to the bottom of the figures.

To quantify the time and length scales of these perturbations, Figure 3a-b shows how the averaged velocity of tracer particles evolves over time, depending on their distance to the meniscus movement (defined as the centre of the maximum inscribed sphere of the pore or throat that underwent the occupancy change). The velocity perturbations caused by both snap-off and CPF are still detectable 21 pore diameters from the displacement, demonstrating the long-ranged character of these events. The onset of the perturbation is rapid in both cases, consistent with the fast nature of these displacements. However, the decay time differs: approximately 2.5 s for snap-off and

5 s for CPF. The velocity perturbation caused by a Haines jump, in the same fluid-fluid pairing and sample type as the experiments presented here, has been shown to decay over approximately 10 s (Bultreys et al., 2024). While solid conclusions would require statistical analysis for which the data is currently lacking, these observations suggest that the duration of velocity decay for individual displacements appears to be largest for Haines jumps, followed by CPF and snap-off. This hierarchy would be consistent with the volumes of fluid displaced by each event, since snap-offs displace smaller volumes than CPF events (Singh et al., 2017), which in turn displace smaller volumes than Haines jumps involving cascading events across several pores (Berg et al., 2013). The two-orders-of-magnitude difference between our measured time scales and those reported in micromodel studies at similar Ca (Armstrong et al., 2015) is attributable to the commensurately lower viscosity of the nonwetting phase used in those studies.

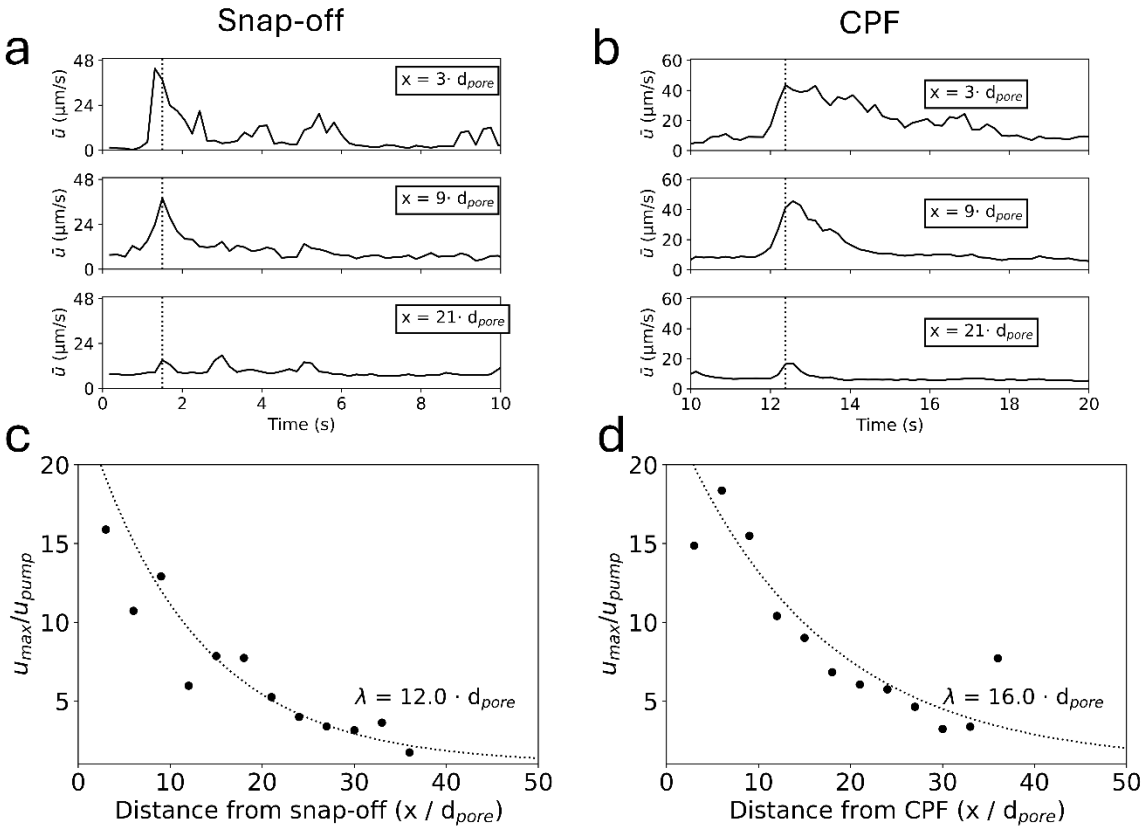


Figure 3: a-b) mean local velocity over time for particles at different distances from the displacement location. The distances are measured in a straight line and expressed as a function of pore diameter. The dotted lines indicate the moment the snap-off or CPF commenced. c-d) The normalised maximum local mean velocity (peaks at/immediately after the displacements, obtained from a-b) as a function of distance from the displacement. The decay is a result of viscous dissipation and geometric dilution. The characteristic decay length is 12 and 16 pore diameters for the snap-off and CPF respectively.

Near the displacement, mean flow velocities exceed 15 times the injection flow rate, and even at distances of 20 pore diameters, velocities remain approximately five times greater than the injection rate (Figure 3c-d). These elevated local flow rates may affect the balance of capillary, viscous, and inertial forces. It is important to note that the fastest velocities during pore filling and snap-off are likely missed, because motion

blurring prevents tracking of particles faster than 58.7 μm/s in the capillary fingering experiment and 29.3 μm/s in the transition-zone and near-stable displacement experiments, based on the imaging speeds. The peak amplitude of the capillary-driven fluctuations is therefore underestimated, although the slower flow response that follows these events is resolved.

To characterise the zone for which this may play a role, we investigate the length scale over which velocity fluctuations decay. Figure 3c-d show that the maximum velocity perturbation decays exponentially over a characteristic length (λ) of 12 pore diameters for snap-off and 16 pore diameters for CPF. Both values are an order of magnitude larger than the characteristic pore size and are comparable to the λ = 14.7 pore diameters reported for drainage Haines jumps (Bultreys et al., 2024).

2.3. Shear and recirculating flows are correlated to ganglion dynamics in the transition regime

In the near-stable displacement experiment, the nonwetting phase is not displaced in a localise or compact front as expected, but is rather characterised by highly dynamic, fragmented ganglia that are continually remobilised, split and re-trapped throughout the pore space (Figure 4). The transition-zone experiment shows more localise pore filling dynamics with limited ganglion dynamics. Overall, this suggests that regimes and regime boundaries derived mainly from 2D micromodel observations, as in Figure 1, may not transfer directly to the more complex pore spaces of 3D media.

While individual ganglion mobilisation and break-up are fairly well understood, the collective dynamics across many ganglia in a 3D porous medium have remained unclear. Individual ganglion dynamics arise when viscous drag exerted by the flowing wetting phase exceeds the capillary forces that resist ganglion breakup or throat entry (Datta, Ramakrishnan, et al., 2014). To examine the collective dynamics, we focus on the near-stable displacement experiment, which offers the richest set of ganglion events in our dataset. The high temporal resolution of our experiments reveals that mobilisation events cascade through the pore space: ganglia that appear stably trapped suddenly start to move, likely in response to changes in the surrounding wetting-phase flow when other ganglia are displaced (V4). Mobilisation is commonly accompanied by ganglion splitting, which can either precede or follow it. There are on average 2.5 ganglion break-ups per second, resulting in 3% of all ganglia experiencing at least one break-up event during the experiment (58 ganglia of 1951 total ganglia).The time interval between break-ups of individual ganglia spans the entire experiment (Figure 5d), reflecting the remobilisation events in function of changes in the surrounding flow field. Consequently, part of the remobilised nonwetting volume is typically re-trapped before it leaves the field of view (Figure 4).

As a result of ganglion dynamics, the number of distinct ganglia increases by 50%, despite a monotonic decrease in the nonwetting phase saturation (Figure 5a,c). The mean ganglion size decreases over time and then approaches a plateau (Figure 5c).

This agrees with Rücker et al. (2015), who observed a rapid drop in saturation once remobilisation began, together with a sharp rise in the number of newly formed clusters, followed by a similar plateau. Mean ganglion velocity (Figure 5b), while noisy, follows the same trend, plateauing at the same stage as the total number of ganglia. This indicates that the nonwetting phase becomes more static as the experiment proceeds.

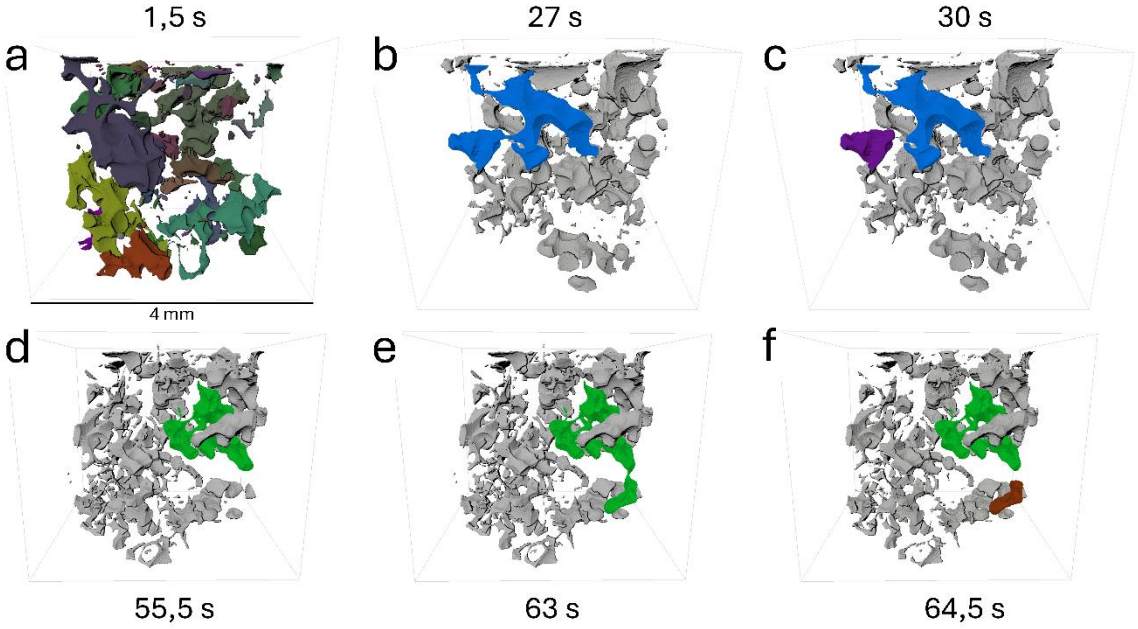


Figure 4: visualisation of distinct nonwetting phase ganglia over six different points in time. The wetting phase and solid grains are transparent. a) Nonwetting phase at the start of the experiment. Individual ganglia have distinct colours to provide a qualitative visualisation of connectivity. b-c) the blue parent ganglion snaps off into two daughter ganglia (blue and purple). The nonwetting phase not involved with this displacement is shown in grey. d-f) the green ganglion remobilises and then snaps off into two daughter ganglia (green and brown). The nonwetting phase not involved with this displacement is shown in grey. Flow direction is from the top to the bottom of the page.

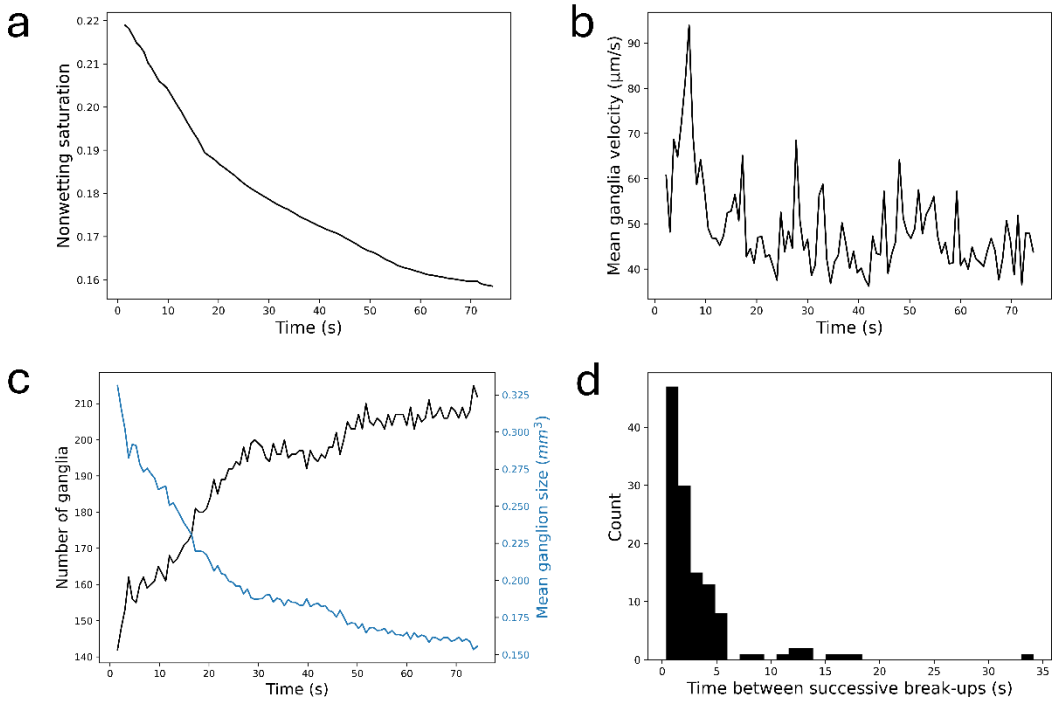


Figure 5: a) nonwetting phase saturation; b) mean ganglia velocity throughout the sample; c) number of nonwetting ganglia and mean ganglion size over time; and d) time between successive ganglion break-ups.

To characterise the structure of the 3D flow field inside the collection of ganglia, we calculate the flow-type parameter field (ξ) for the near-stable displacement experiment (Astarita, 1979). This parameter, originally developed to classify flows of non-Newtonian fluids, compares the local magnitudes of strain rate and vorticity to characterise whether a fluid element undergoes rotation, simple shear or pure extension, independent of flow magnitude. Figure 6 shows a 3D rendering and a 2D cross-section of this parameter for one trapped ganglion at an immobile time point. The external layer of the ganglion is shear-dominated ($\xi \approx 0$), while the interior exhibits a strong rotational flow centre ($\xi < 0$) with surrounding vortex flow. Rotational flow patterns arise as a signature of recirculation: if momentum is transferred across the menisci but the ganglion is immobile, the flow must be recirculating to incur a net zero ganglion displacement (Mansouri-Boroujeni et al., 2023; Roman et al., 2016, 2020; Sharma et al., 2022; Zarikos et al., 2018). To investigate the origin of the shear layer, we calculate the tracers' velocity component tangential to fluid menisci in function of distance to the nearest meniscus point. Figure S5 shows that these velocities are elevated near the meniscus and decay with increasing distance, plateauing at approximately one-third of a pore diameter from the meniscus. This reveals substantial shear flow acting across the menisci, agreeing qualitatively with 2D micromodel studies (Sharma et al., 2022; Zarikos et al., 2018). The tangential velocity peak is absent in the capillary fingering experiment (Figure S5), confirming that interfacial drag

is negligible in this experiment, due to the far lower viscosity of the invading phase relative to the trapped phase.

The temporal evolution of the trapped ganglion's mean ξ suggests two dynamic states (Figure 6c). During immobile intervals, mean ξ is lower, consistent with shear and recirculatory flow driven by interfacial drag from the flowing wetting phase. The onset of mobile intervals is correlated with elevated tangential velocities (Figure S5), stressing the importance of shear flow on ganglion remobilisation. During these events, mean ξ increases, indicating a shift towards extensional flow. This is consistent with elongational deformation as the ganglion body advances through converging and diverging pore geometries, stretching fluid elements as they accelerate into throats or as daughter ganglia separate.

A similar trend is observed in the mean ξ across all ganglia, which is positive and decreases over time (Figure 6). This suggests a shift from elongationally-dominated flow towards shear and rotational flow over the course of the experiment. The early elongational flow is consistent with the prevalence of mobile and splitting ganglia. In contrast, as ganglia become smaller and less mobile over the course of the experiment, the internal flow becomes dominated by tangential interfacial drag, producing shear and recirculation (Figure 1 - 3).

It should be noted that our method was not able to track particles moving faster than 29.3 μm/s, which degrades the velocity field during fast ganglion motions. More generally, ξ is computed from interpolated velocity fields and tends towards positive values where tracer particle detections are sparse, as occurs when fast particles are lost or early in the experiment. This may lead to errors in the calculation of ξ at these moments, particularly by overestimating elongational flow. The increases in ξ during mobile events and the early elongational regime should therefore be interpreted qualitatively, while rotation-dominated regions ($\xi < 0$), which require locally dense particle data, are the most robust features.

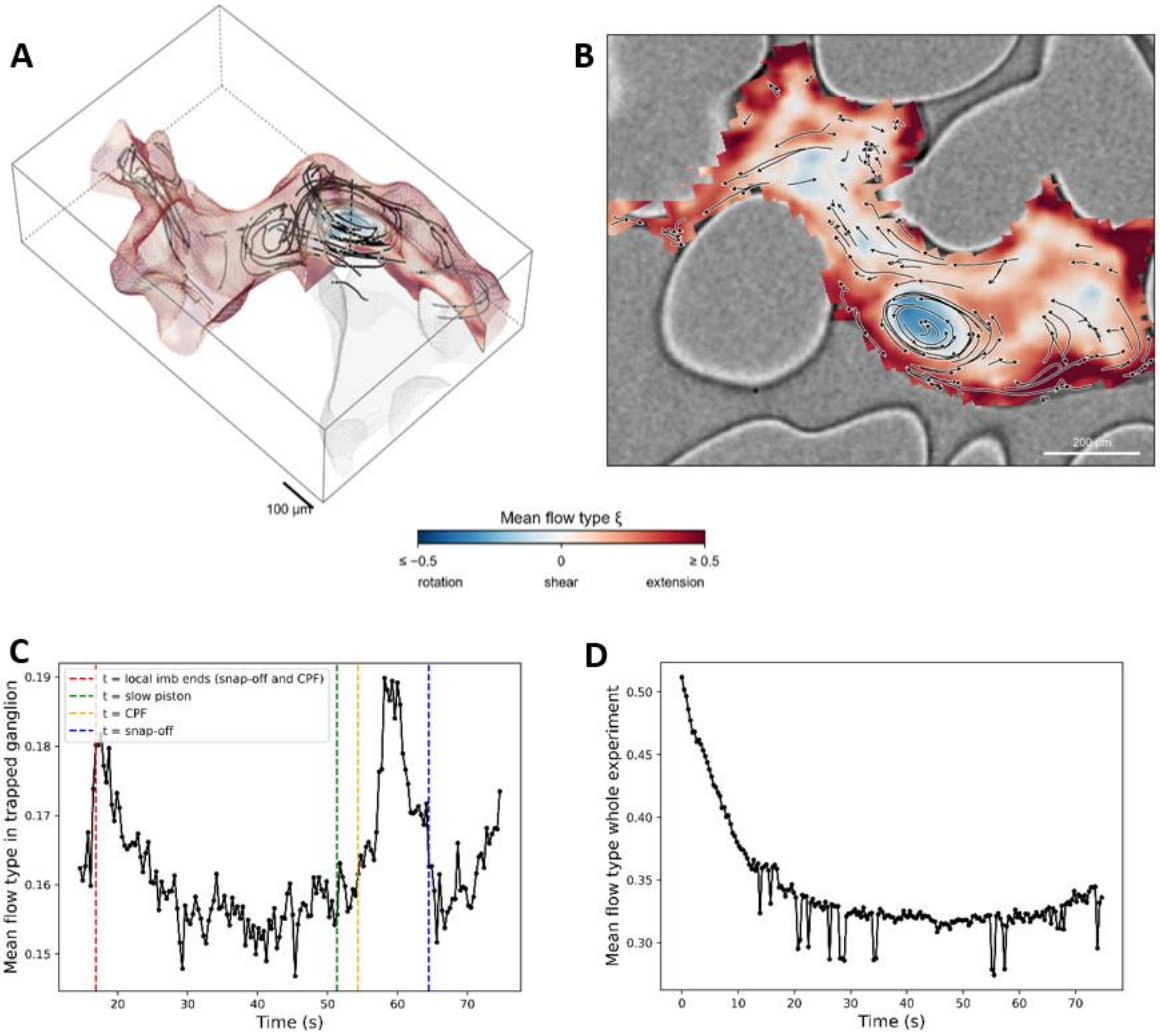


Figure 6: local flow type within a trapped ganglion in A) 3D and B) a 2D cross-section, highlighting a rotation centre. 0.5 (red) indicates extensional flow, 0 (white) indicates shear-dominated flow and -0.5 (blue) indicates rotational flow. C) the mean flow type within the trapped ganglion over the experiment. D) the mean flow type across the entirety of the pore space.

3. Discussion

We used X-ray Particle Tracking Velocimetry to directly measure 3D velocity fields in the nonwetting phase during imbibition experiments in the capillary fingering, transition-zone and near-stable displacement regimes. The experiments span a wide range of capillary number and viscosity ratio, encompassing both capillary-dominated and mixed capillary-viscous behaviour, revealing markedly different internal flow dynamics across these regimes. Notably, the near-stable displacement experiment does not show a compact displacement front, but highly dynamic, fragmented ganglia that are continually mobilised, split and re-trapped throughout the pore space. Ganglion mobilisation is commonly accompanied by ganglion splitting, generating smaller daughter ganglia that may be re-trapped in the pore space. These

observations suggest that regime boundaries derived mainly from 2D micromodels (Primkulov et al., 2021) may not transfer directly to 3D porous media.

In the capillary fingering regime, snap-off and cooperative pore filling generate long-ranged velocity perturbations spanning length scales an order of magnitude larger than the characteristic pore size. Fluids follow tortuous pathways throughout the pore space, similar to the behaviour during drainage Haines jumps (Bultreys et al., 2024). Perturbations from snap-off decay faster (approximately 2.5 s) than those from CPF (approximately 5 s) or Haines jumps (approximately 10 s), consistent with the smaller fluid volumes displaced. Local fluid velocities near the displacement exceed 15 times the injection flow rate and remain approximately five times greater even 20 pore diameters away. These elevated velocities transiently shift the balance of capillary, viscous and inertial forces, and suggest that the characteristic length scale for the REV of multiphase flow is larger than commonly assumed from static fluid distributions alone. These fluctuations may also enhance solute mixing and colloid remobilisation, with implications for groundwater contamination and remediation. We note that velocities close to the events may exceed the maximum trackable tracer velocity in our experiments, and peak amplitudes are hence likely underestimated.

At higher capillary numbers and viscosity ratios near one, flow in the nonwetting phase is no longer dominated by isolated capillary events, but by momentum transmitted from the wetting phase across the fluid–fluid interface. This is important as viscous coupling between the phases affects the relative permeability at the continuum scale (Avraam & Payatakes, 1999; Solazzi et al., 2023). In our experiments, momentum transferred across the menisci drives shear near the interface and complex recirculation patterns within ganglia, in some cases leading to local vortex-like streamlines. To our knowledge, the occurrence of localise recirculation zones within more complex recirculation patterns has not been described in previous experiments, likely because these were performed on 2D micromodels. In 3D porous media, complex ganglion shapes and menisci oriented at varying angles to the flow reduce the directional coherence of the interfacial drag. During mobilisation, this pattern appears to be temporarily replaced by more elongational flow fields, which would stretch the nonwetting phase as it passes through converging-diverging geometries (pore throats). The resistance of a fluid to stretching is captured by the extensional viscosity, which can be orders of magnitude higher than shear viscosity for polymer solutions and other viscoelastic fluids (Petrie, 2006). Such fluids may therefore show delayed breakup and different mobilisation thresholds. Because elongation also stretches fluid elements more efficiently than shear, mobilisation events may be hypothesized to be periods of enhanced internal mixing and interfacial mass transfer (Maeritz et al., 2026; Villermaux, 2019). Elongational flow during mobilisation may therefore be relevant for environmental remediation of non-aqueous pollutants, particularly those with complex rheologies (e.g. heavy petroleum products). Further work, including higher temporal resolution to track fast particles during mobilisation, is needed to confirm this hypothesis.

Collectively, our findings show that internal flow dynamics need to be accounted for when characterising and upscaling multiphase flow. Recent upscaling theories establish that fluctuations must be averaged over both space and time (McClure et al., 2021, 2022). Our results provide the experimental foundation needed to define the relevant scales. Future work may focus on extending the methodology used in this paper to measurements in the wetting phase, so that the full momentum balance may be probed. Improvements in temporal resolution will be needed to fully characterise velocities of fast-moving ganglia, which are currently undersampled by the method. More broadly, our results show that measuring the flow field itself, rather than only the fluid distribution, reveals pore-scale dynamics that are not captured by conventional imaging and may ultimately help connect them to continuum-scale descriptions of multiphase flow.

4. Materials and methods

4.1. Materials

To conduct these imbibition experiments, the nonwetting phase was seeded with X-ray attenuating particles. This allowed for the direct measurement of flow fields within the nonwetting phase during unsteady displacements. Imbibition was produced by either injecting the wetting phase or by withdrawing the nonwetting phase from the samples.

Three imbibition experiments were conducted on cylindrical samples of sintered glass filter (ROBU PO, Germany), 4 mm in diameter and 10 mm in length, in a setup that enabled continuous imaging with synchrotron X-ray micro-CT while fluids were injected or retracted. The samples were mounted in a Hassler-type flow cell (RS systems, Norway) and connected to a syringe pump mounted on the beam line's rotation stage (Harvard Apparatus, USA). To prepare the samples for the experiment, they were initially saturated with a wetting fluid (different water-glycerol mixtures doped with KI for image contrast), after which a nonwetting fluid (silicone oil AR200, Sigma-Aldrich) was injected. The properties of the fluids used in the three experiments are listed in Table 1. Prior to the experiment, the absolute pore pressure was raised to counteract bubble formation from ionising radiation during imaging (21.5 bar for the capillary fingering experiment; 30 bar for the transition-zone and near-stable displacement experiments). Then, the imbibition experiment was conducted by retracting the silicone oil from the sample in the case of the capillary fingering experiment, or by injecting wetting fluid in the case of the transition-zone and near-stable displacement experiments, while acquiring micro-CT images (Section 4.2).

The nonwetting phase in all experiments was seeded with hollow silver-coated glass spheres (CoSpheric, USA; mean diameter 10 μm; density 1.08 kg/l) at 1.18 vol%, serving as X-ray attenuating tracer particles. The density of the tracer particles closely matches that of the silicone oil (1.07 kg/l), minimising gravitational settling and

centrifugal effects during sample rotation. The silicone oil and particle mixture was treated with an ultrasonic homogeniser (Hielscher UP50H, Germany) to prevent agglomeration and then placed in an ultrasonic bath (Bandelin Sonorex TK52, Germany). Wetting phase solutions were degassed under vacuum prior to use.

The mean pore diameter of the sintered porous glass samples is 84, 106 and 108 μm and the porosity is 0.27, 0.28 and 0.31 respectively, determined from segmented three-dimensional micro-CT images of the dry samples using the pore network extraction code pnextract (Raeini et al., 2017).

We estimated the balance of forces in the experiments with two commonly used dimensionless parameters: the capillary number $Ca = v\mu/\sigma$; and the viscosity ratio $M = \mu_{invading}/\mu_{displaced}$; where v is the Darcy velocity of the invading fluid, μ its viscosity, and σ the interfacial tension, and $\mu_{invading}$ and $\mu_{displaced}$ the viscosities of the invading and displaced fluid. The Ca, M and flow regime classification following Primkulov et al. (2021) are summarised in Table 2. The two experiments at elevated Ca ($Ca \sim 10^{-5}$ and $Ca \sim 10^{-4}$) were designed to investigate the transition between the capillary fingering and stable displacement regimes. The former is referred to here as the "transition-zone experiment" and the latter as the "near-stable displacement experiment", reflecting their positions within the phase diagram.

Table 1: Fluid properties.

Fluid	Composition	Density (kg/l)	Viscosity (mPa s)
KI-brine	8 wt% KI	1.09	1
KI-glycerol-brine	91 wt% glycerol, 6 wt% KI	1.23	183
Silicone oil AR200	Pure	1.07	200

Table 2: Experiment parameters.

Flow regime	Fluid pair	Wetting / nonwetting phases	Viscosity ratio (M)	Capillary number (Ca)	Flow rate (μl/min)	Interstitial velocity (μm/s)
Capillary fingering	KI-brine / silicone oil	Wetting: KI-brine; nonwetting: silicone oil	0.005	1.6×10^{-8}	0.6	2.95
Transition zone	KI-glycerol-brine / silicone oil	Wetting: KI-glycerol-brine; nonwetting: silicone oil	0.915	9.32×10^{-5}	19.2	90.9

Near-stable displacement	KI-glycerol-brine / silicone oil	Wetting: KI-glycerol-brine; nonwetting: silicone oil	0.915	3.73×10^{-4}	76.8	328.6

4.2. Synchrotron imaging and image reconstruction

Time series of 3D images were acquired for each imbibition experiment, using the TOMCAT beamline of the Swiss Light Source (Paul Scherrer Institute, Switzerland). For the capillary fingering experiment, 130 tomograms of 0.1875 s each were acquired over 24.4 s (each tomogram consisting of 500 radiographs at 0.375 ms exposure). For the transition-zone and near-stable displacement experiments, 200 tomograms of each 0.375 s were acquired over 75 s (500 radiographs at 0.75 ms exposure). The voxel size was 2.75 µm for all experiments.

The imaging was performed using the GigaFRoST high-speed camera and 4x optical magnification (Optique Peter) (Bührer et al., 2019; Mokso et al., 2017) and a maximum field of view of 5.5 x 5.5 mm^2. The X-ray beam was filtered with 5 mm glass carbon and 4 mm borosilicate glass. Each tomogram was reconstructed twice from radiographs taken over 180° using the gridrec algorithm (Marone & Stampanoni, 2012): once using Paganin phase retrieval (Paganin et al., 2004) to maximise contrast between nonwetting and wetting phases for segmentation, and once without phase retrieval to maximise contrast between tracer particles and the surrounding oil for particle detection.

4.3. X-ray Particle Tracking Velocimetry

Individual particles were tracked through the reconstructed time series using a Lagrangian algorithm described in detail in Bultreys et al. (2022, 2024). Minor misalignments between consecutive tomograms were corrected by image registration using SimpleITK (Lowekamp et al., 2013) in Python prior to tracking. Background subtraction and pore space segmentation were performed in Fiji (Schindelin et al., 2012) and Python (Section 4.5). Particles were identified in each tomogram as local grey-value minima using the open-source package TrackPy (Allan et al., 2021), with a minimum inter-particle distance of four voxels. Particle identifications were linked to form particle trajectories using a nearest-neighbour approach. Trajectories spanning fewer than 20 consecutive timesteps were discarded as noise. A time-varying segmentation mask of the nonwetting phase was used to exclude spurious detections in the wetting phase. Particle velocities were computed using second-order finite differences across consecutive detections, resulting in a point cloud of velocities per timestep.

Bultreys et al. (2022) found that the particle tracking approach used here yields reliable velocities for particles moving up to 4 voxels/frame. In these experiments, this equates to 58.7 µm/s in the capillary fingering regime experiment and 29.3 µm/s in the

transition-zone and near-stable displacement experiments. Faster-moving particles are not reliably detected due to motion artefacts deforming particle shapes and reducing contrast with the surrounding fluid, leading to an underestimation of velocities in the transition-zone and near-stable displacement regime experiments. A more detailed examination of uncertainties in the particle tracking is given in the supplementary material.

4.4. Velocity field analysis

Tangential velocities, the magnitudes of the particle velocity component parallel to the nearest fluid meniscus, were calculated to quantify the effects of interfacial drag. The meniscus surface was extracted from the phase segmentation and surface normals computed using PyVista (Sullivan et al., 2023). For each particle, the nearest meniscus point was located using a kd-tree (SciPy) (Virtanen et al., 2020), and the velocity was decomposed into components parallel and perpendicular to the meniscus using the surface normal. The magnitude of the parallel component constitutes the tangential velocity.

To obtain 3D velocity fields, the velocity point clouds were interpolated using natural-neighbour interpolation (Sibson, 1981) onto a regular grid matching the resolution of the tomograms, and then downsampled by a factor of 8 to reduce computational demand. Stationary particles were randomly seeded along the grain boundaries to impose no-slip boundary conditions.

The interpolated 3D velocity fields were used to compute the strain rate and vorticity, which are used to determine the flow type parameter, ξ (Astarita, 1979). The strain rate was determined from the gradient of the velocity field calculated using central differences. The vorticity was calculated as the curl of the velocity vector. Renderings of the strain rate, viscous dissipation and vorticity fields are shown individually in supplementary material.

The flow type parameter indicates the dominant patterns present in the 3D flow field, from purely rotational flow ($\xi = -1$), through simple shear ($\xi = 0$), and purely extensional flow ($\xi = 1$). It was computed as $\xi = (\|E\| - \|\Omega\|) / (\|E\| + \|\Omega\|)$, where $E = \frac{1}{2}(\nabla u + \nabla u^{\mathsf{T}})$ is the strain-rate tensor, $\Omega = \frac{1}{2}(\nabla u - \nabla u^{\mathsf{T}})$ is the vorticity tensor, and $\|\cdot\|$ denotes the Frobenius norm.

4.5. Image segmentation and ganglia tracking

To identify the two fluid phases in each of the time series images, nonwetting phase segmentations were obtained by subtracting registered wetting-saturated reference images from the time-resolved experimental images, followed by Otsu thresholding, morphological opening and hole-filling operations in Python. Further despeckling was performed in Avizo (Thermo Fisher Scientific). For the near-stable displacement experiment, connected-component labelling was applied at each timestep to identify individual ganglia, and a greedy tracking algorithm was used to follow ganglia through time, detecting splitting (snap-off) and coalescence events based on volume matching

(within 10%) and bounding-box overlap criteria. The effective ganglion velocity was calculated from the displacement of the centre of mass of each tracked ganglion between timesteps. Details on the segmentation method and the ganglia tracking algorithm can be found in the supplementary material.

Data, Materials, and Software Availability

The 6 TB tomography dataset will be made available in the PSI Public Data Repository upon publication. The code used to analyse the images and resulting derived data (particle tracking, ganglia tracking, velocity field analysis) will be made available on Github upon publication.

Acknowledgements

T.B. acknowledges funding from the European Union (ERC Starting Grant, FLOWSCOPY, 101116228) and from the Research Foundation- Flanders (FWO, senior research fellowship 12X0922N). S.E. acknowledges funding from the FWO under Grant 1182822N and G065224N. We acknowledge partial funding from FWO under research projects G051418N and G004820N and the UGent BOF funding for the Centre for X-ray Tomography (BOF.COR.2022.008) and IOF, project FaCT F2021/IOF-Equip/021. We acknowledge the Paul Scherrer Institute, Villigen, Switzerland for provision of synchrotron radiation beamtime at the TOMCAT beamline X02DA of the SLS (beam time proposal 20222039).

References

Allan, D. B., Caswell, T., Keim, N. C., der Wel, C. M., & Verweij, R. W. (2021, April). soft-matter/trackpy: Trackpy v0.5.0. Zenodo. https://doi.org/10.5281/zenodo.4682814

Armstrong, R. T., Georgiadis, A., Ott, H., Klemin, D., & Berg, S. (2014). Critical capillary number: Desaturation studied with fast X-ray computed microtomography. *Geophysical Research Letters*, *41*(1), 55–60. https://doi.org/10.1002/2013GL058075

Armstrong, R. T., Evseev, N., Koroteev, D., & Berg, S. (2015). Modeling the velocity field during Haines jumps in porous media. *Advances in Water Resources*, *77*, 57–68. https://doi.org/10.1016/j.advwatres.2015.01.008

Armstrong, R. T., McClure, J. E., Berrill, M. A., Rücker, M., Schlüter, S., & Berg, S. (2016). Beyond Darcy's law: The role of phase topology and ganglion dynamics for two-fluid flow. *Physical Review E*, *94*(4). https://doi.org/10.1103/PhysRevE.94.043113

Astarita, G. (1979). Objective and generally applicable criteria for flow classification. *Journal of Non-Newtonian Fluid Mechanics*, *6*, 69–76.

Avraam, D. G., & Payatakes, A. C. (1995a). Flow regimes and relative permeabilities during steady-state two-phase flow in porous media. *Journal of Fluid Mechanics*, *293*(2), 207–236. https://doi.org/10.1017/S0022112095001698

Avraam, D. G., & Payatakes, A. C. (1995b). Generalized relative permeability coefficients during steady-state two-phase flow in porous media, and correlation with the flow mechanisms. *Transport in Porous Media*, *20*(1–2), 135–168. https://doi.org/10.1007/BF00616928

Avraam, D. G., & Payatakes, A. C. (1999). Flow mechanisms, relative permeabilities, and coupling effects in steady-state two-phase flow through porous media. The case of strong wettability. *Industrial and Engineering Chemistry Research*, *38*(3), 778–786. https://doi.org/10.1021/ie980404o

Berg, S., Ott, H., Klapp, S. A., Schwing, A., Neiteler, R., Brussee, N., et al. (2013). Real-time 3D imaging of Haines jumps in porous media flow. *Proceedings of the National Academy of Sciences*, *110*(10), 3755–3759. https://doi.org/10.1073/pnas.1221373110

Bührer, M., Stampanoni, M., Rochet, X., Büchi, F., Eller, J., & Marone, F. (2019). High-numerical-aperture macroscope optics for time-resolved experiments. *Journal of Synchrotron Radiation*, *26*, 1161–1172. https://doi.org/10.1107/S1600577519004119

Bultreys, T., Van Offenwert, S., Goethals, W., Boone, M. N., Aelterman, J., & Cnudde, V. (2022). X-ray tomographic micro-particle velocimetry in porous media. *Physics of Fluids*, *34*(4), 42008. https://doi.org/10.1063/5.0088000

Bultreys, T., Ellman, S., Schlepütz, C. M., Boone, M. N., Pakkaner, G. K., Wang, S., et al. (2024). 4D microvelocimetry reveals multiphase flow field perturbations in porous media. *Proceedings of the National Academy of Sciences*, *121*(12). https://doi.org/10.1073/pnas.2316723121

Datta, S. S., Dupin, J. B., & Weitz, D. A. (2014). Fluid breakup during simultaneous two-phase flow through a three-dimensional porous medium. *Physics of Fluids*, *26*(6), 1–13. https://doi.org/10.1063/1.4884955

Datta, S. S., Ramakrishnan, T. S., & Weitz, D. A. (2014). Mobilization of a trapped non-wetting fluid from a three-dimensional porous medium. *Physics of Fluids*, *26*(2), 1–22. https://doi.org/10.1063/1.4866641

Gao, Y., Lin, Q., Bijeljic, B., & Blunt, M. J. (2017). X-ray Microtomography of Intermittency in Multiphase Flow at Steady State Using a Differential Imaging Method. *Water Resources Research*, *53*(12), 10274–10292. https://doi.org/10.1002/2017WR021736

Guo, F., & Aryana, S. A. (2019). An experimental investigation of flow regimes in imbibition and drainage using a microfluidic platform. *Energies*, *12*(7). https://doi.org/10.3390/en12071390

Guo, H., Song, K., & Hilfer, R. (2022). A Brief Review of Capillary Number and its Use in Capillary Desaturation Curves. *Transport in Porous Media*, *144*(1), 3–31. https://doi.org/10.1007/s11242-021-01743-7

Krevor, S., Blunt, M. J., Benson, S. M., Pentland, C. H., Reynolds, C., Al-Menhali, A., & Niu, B. (2015). Capillary trapping for geologic carbon dioxide storage - From pore scale physics to field scale implications. *International Journal of Greenhouse Gas Control*, *40*, 221–237. https://doi.org/10.1016/j.ijggc.2015.04.006

Lenormand, R, Touboul, E., & Zarcone, C. (1988). Numerical models and experiments on immiscible displacements in porous media. *J. Fluid Mech*, *189*, 165–187.

Lenormand, Roland, & Zarcone, C. (1984). Role of roughness and edges during imbibition in square capillaries. *Proceedings - SPE Annual Technical Conference and Exhibition*, *1984-Septe*. https://doi.org/10.2523/13264-ms

Liu, H., Zhang, Y., & Valocchi, A. J. (2015). Lattice boltzmann simulation of immiscible fluid displacement in porous media: Homogeneous versus heterogeneous pore network. *Physics of Fluids*, *27*(5). https://doi.org/10.1063/1.4921611

Lowekamp, B. C., Chen, D. T., Ibáñez, L., & Blezek, D. (2013). The Design of SimpleITK. *Frontiers in Neuroinformatics*, *7*. https://doi.org/10.3389/fninf.2013.00045

Ma, J., Li, Q., Kühn, M., & Nakaten, N. (2018). Power-to-gas based subsurface energy storage: A review. *Renewable and Sustainable Energy Reviews*, *97*(January), 478–496. https://doi.org/10.1016/j.rser.2018.08.056

Maeritz, M., Le Borgne, T., Lester, D. R., & Heyman, J. (2026). Shear versus stretching as drivers for mixing in three-dimensional porous media flows. *Physical Review Fluids*, *11*(9), 094501. https://doi.org/10.1103/4wyw-nkrb

Mansouri-Boroujeni, M., Soulaine, C., Azaroual, M., & Roman, S. (2023). How interfacial dynamics controls drainage pore-invasion patterns in porous media. *Advances in Water Resources*, *171*. https://doi.org/10.1016/j.advwatres.2022.104353

Marone, F., & Stampanoni, M. (2012). Regridding reconstruction algorithm for real-time tomographic imaging. *Journal of Synchrotron Radiation*, *19*(6), 1029–1037. https://doi.org/10.1107/S0909049512032864

McClure, J. E., Berg, S., & Armstrong, R. T. (2021). Thermodynamics of fluctuations based on time-and-space averages. *Physical Review E*, *104*(3), 28–36. https://doi.org/10.1103/PhysRevE.104.035106

McClure, J. E., Fan, M., Berg, S., Armstrong, R. T., Berg, C. F., Li, Z., & Ramstad, T. (2022). Relative permeability as a stationary process: Energy fluctuations in immiscible displacement. *Physics of Fluids*, *34*(9), 092011. https://doi.org/10.1063/5.0107149

Mokso, R., Schlepütz, C. M., Theidel, G., Billich, H., Schmid, E., Celcer, T., et al. (2017). GigaFRoST: The gigabit fast readout system for tomography. *Journal of Synchrotron Radiation*, *24*(6), 1250–1259. https://doi.org/10.1107/S1600577517013522

Paganin, D., Gureyev, T. E., Pavlov, K. M., Lewis, R. A., & Kitchen, M. (2004). Phase retrieval using coherent imaging systems with linear transfer functions. *Optics Communications*, *234*(1–6), 87–105. https://doi.org/10.1016/j.optcom.2004.02.015

Pak, T., Luz, L. F. de L., Tosco, T., Costa, G. S. R., Rosa, P. R. R., & Archilha, N. L. (2020). Pore-scale investigation of the use of reactive nanoparticles for in situ remediation of contaminated groundwater source. *Proceedings of the National Academy of Sciences*, *117*(24), 13366–13373. https://doi.org/10.1073/pnas.1918683117

Primkulov, B. K., Pahlavan, A. A., Fu, X., Zhao, B., MacMinn, C. W., & Juanes, R. (2021). Wettability and Lenormand's diagram. *Journal of Fluid Mechanics*, *923*. https://doi.org/10.1017/jfm.2021.579

Raeini, A. Q., Bijeljic, B., & Blunt, M. J. (2017). Generalized network modeling: Network extraction as a coarse-scale discretization of the void space of porous media. *Physical Review E*, *96*(1). https://doi.org/10.1103/PhysRevE.96.013312

Roman, S., Soulaine, C., AlSaud, M. A., Kovscek, A., & Tchelepi, H. (2016). Particle velocimetry analysis of immiscible two-phase flow in micromodels. *Advances in Water Resources*, *95*, 199–211. https://doi.org/10.1016/j.advwatres.2015.08.015

Roman, S., Soulaine, C., & Kovscek, A. R. (2020). Pore-scale visualization and characterization of viscous dissipation in porous media. *Journal of Colloid and Interface Science*, *558*, 269–279. https://doi.org/10.1016/j.jcis.2019.09.072

Rücker, M., Berg, S., Armstrong, R. T., Georgiadis, A., Ott, H., Schwing, A., et al. (2015). From connected pathway flow to ganglion dynamics. *Geophysical Research Letters*, *42*(10), 3888–3894. https://doi.org/10.1002/2015GL064007

Ruspini, L. C., Farokhpoor, R., & Øren, P. E. (2017). Pore-scale modeling of capillary trapping in water-wet porous media: A new cooperative pore-body filling model. *Advances in Water Resources*, *108*, 1–14. https://doi.org/10.1016/j.advwatres.2017.07.008

Schindelin, J., Arganda-Carreras, I., Frise, E., Kaynig, V., Longair, M., Pietzsch, T., et al. (2012). Fiji: an open-source platform for biological-image analysis. *Nature Methods*, *9*(7), 676–682. https://doi.org/10.1038/nmeth.2019

Schlüter, S, Berg, S., Rücker, M., Armstrong, R. T., Vogel, H.-J., Hilfer, R., & Wildenschild, D. (2016). Pore-scale displacement mechanisms as a source of hysteresis for two-phase flow in porous media. *Water Resources Research*, *52*(3), 2194–2205. https://doi.org/https://doi.org/10.1002/2015WR018254

Schlüter, Steffen, Berg, S., Li, T., Vogel, H.-J., & Wildenschild, D. (2017). Time scales of relaxation dynamics during transient conditions in two-phase flow. *Water Resources Research*, *53*(6), 4709–4724. https://doi.org/https://doi.org/10.1002/2016WR019815

Sharma, V. K., Bhowmik, R., Tiwari, P., & Singh, A. (2022). Pore-scale investigation of immiscible fluid displacement process in randomly distributed bead-based porous micromodels using Micro-PIV. *Journal of Petroleum Science and Engineering*, *212*. https://doi.org/10.1016/j.petrol.2022.110301

Sibson, R. (1981). A Brief Description of Natural Neighbor Interpolation. In V. Barnett (Ed.), *Interpreting Multivariate Data* (pp. 21–36). John Wiley & Sons.

Singh, K., Menke, H., Andrew, M., Lin, Q., Rau, C., Blunt, M. J., & Bijeljic, B. (2017). Dynamics of snap-off and pore-filling events during two-phase fluid flow in permeable media. *Scientific Reports*, *7*(1), 1–13. https://doi.org/10.1038/s41598-017-05204-4

Singh, K., Bultreys, T., Raeini, A. Q., Shams, M., & Blunt, M. J. (2022). New type of pore-snap-off and displacement correlations in imbibition. *Journal of Colloid and Interface Science*, *609*, 384–392. https://doi.org/10.1016/j.jcis.2021.11.109

Solazzi, S. G., Jougnot, D., Rubino, J. G., & Holliger, K. (2023). Dynamic Relative Permeabilities for Partially Saturated Porous Media Accounting for Viscous Coupling Effects: An Analytical Solution. *Transport in Porous Media*, *147*(3), 653–677. https://doi.org/10.1007/s11242-023-01920-w

Spurin, C., Bultreys, T., Bijeljic, B., Blunt, M. J., & Krevor, S. (2019a). Intermittent fluid connectivity during two-phase flow in a heterogeneous carbonate rock. *Physical Review E*, *100*(4). https://doi.org/10.1103/PhysRevE.100.043103

Spurin, C., Bultreys, T., Bijeljic, B., Blunt, M. J., & Krevor, S. (2019b). Mechanisms controlling fluid breakup and reconnection during two-phase flow in porous media. *Physical Review E*, *100*(4), 043115. https://doi.org/10.1103/PhysRevE.100.043115

Sullivan, B., Kaszynski, A., Koyama, T., Deak, A., MatthewFlamm, Favelier, G., et al. (2023, October). pyvista/pyvista: v0.42.3. Zenodo. https://doi.org/10.5281/zenodo.8415866

Suwandi, N., Jiang, F., & Tsuji, T. (2022). Relative Permeability Variation Depending on Viscosity Ratio and Capillary Number. *Water Resources Research*, *58*(6). https://doi.org/10.1029/2021WR031501

Villermaux, E. (2019). Mixing Versus Stirring. *Annual Review of Fluid Mechanics*, *51*(1), 245–273. https://doi.org/10.1146/annurev-fluid-010518-040306

Virtanen, P., Gommers, R., Oliphant, T. E., Haberland, M., Reddy, T., Cournapeau, D., et al. (2020). SciPy 1.0: fundamental algorithms for scientific computing in Python. *Nature Methods*, *17*(3), 261–272. https://doi.org/10.1038/s41592-019-0686-2

Zarikos, I., Terzis, A., Hassanizadeh, S. M., & Weigand, B. (2018). Velocity distributions in trapped and mobilized non-wetting phase ganglia in porous media. *Scientific Reports*, *8*(1). https://doi.org/10.1038/s41598-018-31639-4

Zhang, C., Oostrom, M., Wietsma, T. W., Grate, J. W., & Warner, M. G. (2011). Influence of viscous and capillary forces on immiscible fluid displacement: Pore-scale experimental study in a water-wet micromodel

demonstrating viscous and capillary fingering. *Energy and Fuels*, *25*(8), 3493–3505. https://doi.org/10.1021/ef101732k

Zhao, B., MacMinn, C. W., Primkulov, B. K., Chen, Y., Valocchi, A. J., Zhao, J., et al. (2019). Comprehensive comparison of pore-scale models for multiphase flow in porous media. *Proceedings of the National Academy of Sciences of the United States of America*, *116*(28), 13799–13806. https://doi.org/10.1073/pnas.1901619116

Supplementary information for "Imbibition in 3D porous media is shaped by long-range capillary- and shear-driven flow-field dynamics"

Sharon Ellman[a,b], Robert van der Merwe[a,b], Sojwal Manoorkar[a,b], Stefanie Van Offenwert[c], Wannes Goethals[a,b], Christian M. Schlepütz[d], Laurenz Schröer[a,b], Tom Bultreys[a,b]

[a]Department of Geology, PProGRess, Ghent University, Ghent, Belgium; [b]Centre for X-ray Tomography (UGCT), Ghent University, Ghent, Belgium; [c]Fluxys, Belgium; [d]Swiss Light Source, Paul Scherrer Institute, Villigen PSI 5232, Switzerland

Corresponding author: Sharon.ellman@ugent.be (S. Ellman)

i. Supplementary videos

Video V1: Snap-off in the capillary fingering experiment. The nonwetting phase (silicone oil) surface is shown as a mesh. Tracer particles are drawn as arrows, scaled in size and coloured by velocity magnitude (colour scale as in Figure 1 of the main text). Every acquired tomogram before and after the snap-off is shown, so consecutive frames are 0.1875 s apart, covering t = 0 to 2.625 s. The width of the bounding box is 4 mm.

Video V2: Cooperative pore filling (CPF) in the capillary fingering experiment. Same visualisation as Video V1. Every acquired tomogram before and after the CPF event is shown (0.1875 s between frames), covering t = 12 to 14.8125 s. The width of the bounding box is 4 mm.

Video V3: Flow paths of tracer particles within a trapped ganglion in the near-stable displacement experiment. The nonwetting phase surface is shown as a mesh, and tracer particles are shown as spheres whose flow paths are drawn in progressively over time. The video starts when the ganglion becomes trapped and ends just before it breaks up. Every second tomogram is shown (0.75 s between frames). The ganglion is approximately 1.6 mm wide.

Video V4: Tracked nonwetting phase ganglia in the near-stable displacement experiment. Individual ganglia identified by the ganglion tracking algorithm are shown in

distinct colours over the full duration of the experiment. Every second tomogram is shown, so consecutive frames are 0.75 s apart. The width of the bounding box is 4 mm.

ii. Ganglion tracking algorithm

Silicone oil segmentations were obtained by subtracting wet scans (containing only wetting fluid) which were pre-registered to the dry scan (containing only air) from the registered experimental images and then performing a simple Otsu thresholding. Noise was removed by opening and fill holes operations in Python. Further noise removal by "despeckling" was performed in Avizo (Thermo Fisher Scientific). Saturation change over time was determined from these images. Instrument malfunction at the synchrotron led to registration issues in the first 4 timesteps of the near-stable displacement experiment, hence these were excluded from further analysis.

In the near-stable displacement experiment, the ganglia analysis was built on these segmentations. At every timestep, connected-component labelling gave each separate ganglion its own label. For every labelled ganglion and timestep, Avizo (Thermo Fisher Scientific) was then used to extract its volume, the coordinates of its centre, and the position and size of its bounding box. These properties served as input to a ganglia tracking algorithm developed for this work, which links ganglia between consecutive timesteps based on their volumes and bounding boxes. The linking is greedy: each assignment is decided from the local situation at that step, rather than by searching for the globally optimal set of assignments over all ganglia, as the Hungarian algorithm would (Kuhn, 1955). This choice keeps the computational cost low. The algorithm consists of the following steps:

- Single matches: first, the algorithm identifies ganglia that persist from timestep t to t+1, i.e. cases where one ganglion at t corresponds to exactly one ganglion at t+1. A ganglion A at t is linked to a ganglion B at t+1 only if their volumes differ by no more than 10 % and the bounding boxes of A and B overlap at least partly.
- Break-ups: after all single matches have been assigned, the algorithm searches for splitting events, in which one ganglion at t corresponds to two ganglia at t+1. Such an event is recorded when the summed volume of the two ganglia at t+1 lies within 10 % of the volume of the ganglion at t and their bounding boxes overlap at least partly with that of the ganglion at t.
- Coalescence: next, merging events, in which two ganglia at t combine into a single ganglion at t+1, are identified using the same criteria of 10 % volume agreement and bounding-box overlap.
- Remaining ganglia: ganglia that cannot be assigned to a single match, a break-up or a coalescence receive new labels, after which the procedure is repeated for the following timestep.

In this way, the algorithm captures both the splitting and the merging of ganglia. For a break-up, the label of the parent ganglion is stored, the larger daughter ganglion inherits this label and the smaller daughter ganglion receives a new one. For a coalescence, the resulting ganglion inherits the label of the larger of the two merging ganglia. Only events involving two ganglia within a single timestep are considered. In addition, ganglia that move so fast that their bounding boxes do not overlap between consecutive timesteps cannot be followed. Figure S1 shows an example of a break-up identified by the algorithm.

iii. Example of a ganglion breakup and particle velocities in near-stable displacement experiment

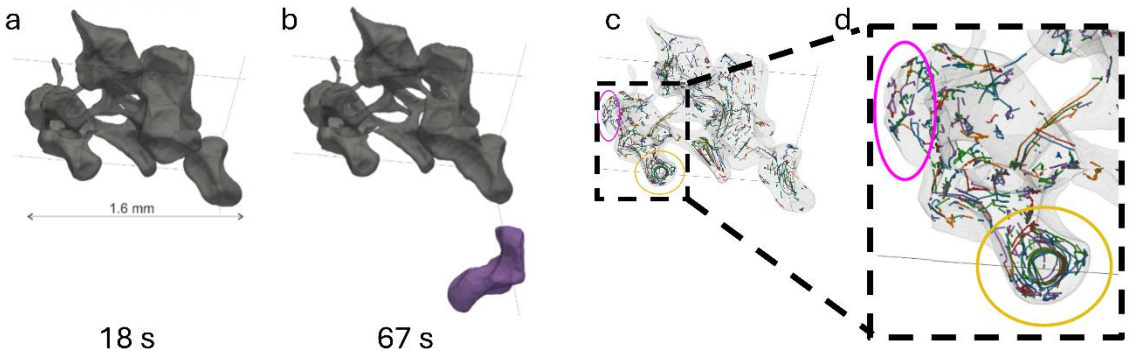


Figure S 1: Visualisations of an initially trapped ganglion which later undergoes snap-off and remobilisation of the smaller daughter ganglion. a) trapped ganglion with static menisci for ~ 37.5 s; b) the ganglion snaps off into two daughter ganglia; c-d) the flow lines within the trapped ganglion for the period over which the menisci are static. The yellow circle highlights a region exhibiting recirculating flows while the pink ellipse highlights shear flows.

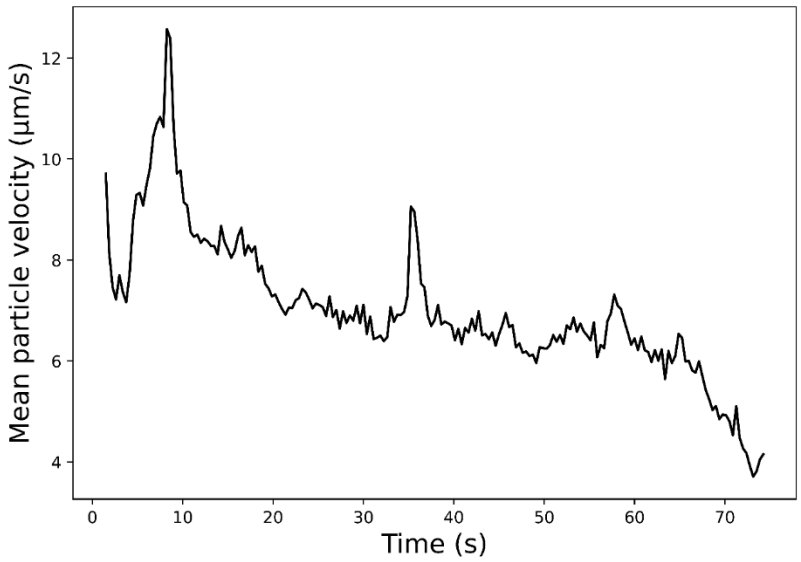


Figure S 2: Mean particle velocities during the near-stable displacement experiment.

iv. Example of a ganglion spanning vortex in a small compact ganglion

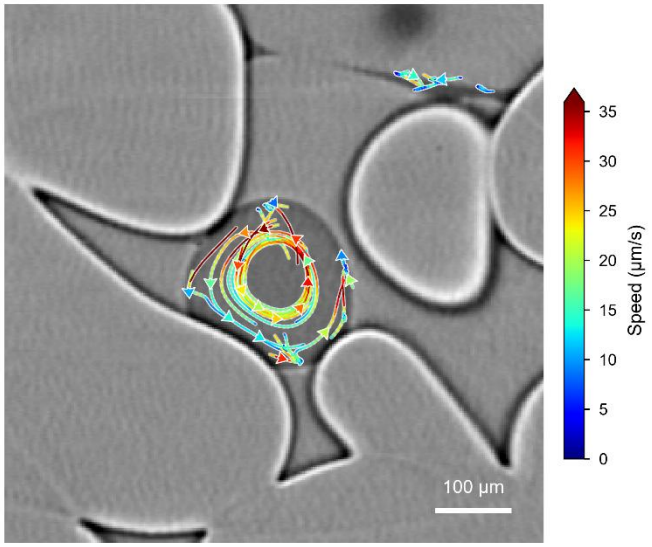


Figure S 3: Example of a vortex in a trapped ganglion. This vortex spans the entire ganglion, as seen in micromodel studies.

v. Uncertainties in the particle tracking

The uncertainties associated with XPTV were quantified in a study by Bultreys et al. (2022), which used a digital twin of an XPTV experiment. Because this digital twin was built from simulated particle trajectories, the tracking results could be benchmarked directly against a known ground truth. The workflow recovered 48% of the ground-truth

particles. Despite this modest detection rate, false positives were rare, making up only 6% of the detections. For particles displaced by less than 4 voxels between frames, the measured positions and velocities were highly accurate. Hence, although a considerable fraction of the particles goes undetected, the positions and trajectories that are retrieved are very likely to be correct.

In our experiments, more than 95% of the detected particles are displaced by less than 4 voxels per frame (Figure S 4), so these detections can be considered reliable. The tracking does, however, break down for fast-moving particles, so many of these are missed, particularly in the near-stable displacement experiment, which has the highest capillary number. The interstitial velocity is a measure of how fast the wetting phase flows through the pore space. In 2D micromodels, recirculating flows inside trapped ganglia were reported to be about ten times slower than the surrounding flowing phase (Zarikos et al., 2018). As the tracer particles are located in the nonwetting phase, their velocities are expected to lie well below the interstitial velocity, particularly inside trapped ganglia, so most of them are likely to be detected. Once a ganglion is remobilised, however, it can move at velocities close to the interstitial velocity, at which point its tracer particles are lost. This is consistent with Figure S 5, in which no velocities close to the interstitial velocity are recorded.

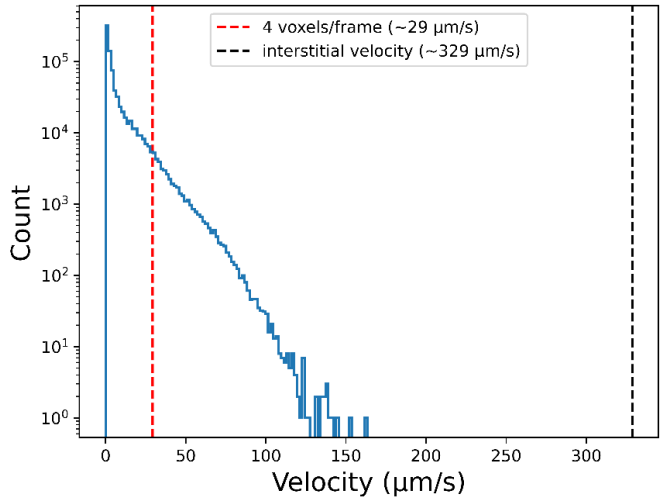


Figure S 4: Distribution of all particle velocities measured in the near-stable displacement experiment. Over 95% of the measured velocities lie under 4 voxels/frame, the limit up to which particle detections are considered reliable.

vi. Tangential particle velocities

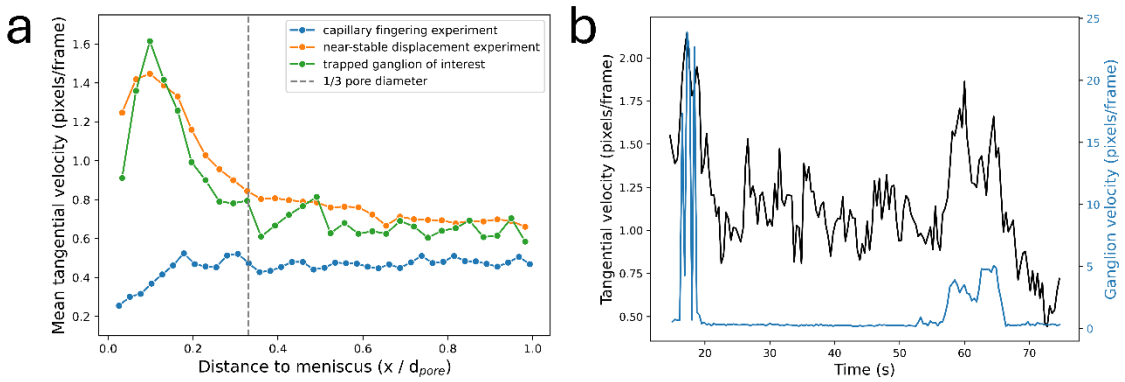


Figure S 5: a) mean tangential velocity versus distance from the meniscus (in pore diameters) for the near-stable displacement experiment (full field of view and trapped ganglion only) and the capillary fingering experiment (as control). b) mean tangential velocity within one-third of a pore diameter from the meniscus of the trapped ganglion (blue) and effective ganglion velocity (orange) versus time.

vii. Strain rate, viscous dissipation and vorticity fields

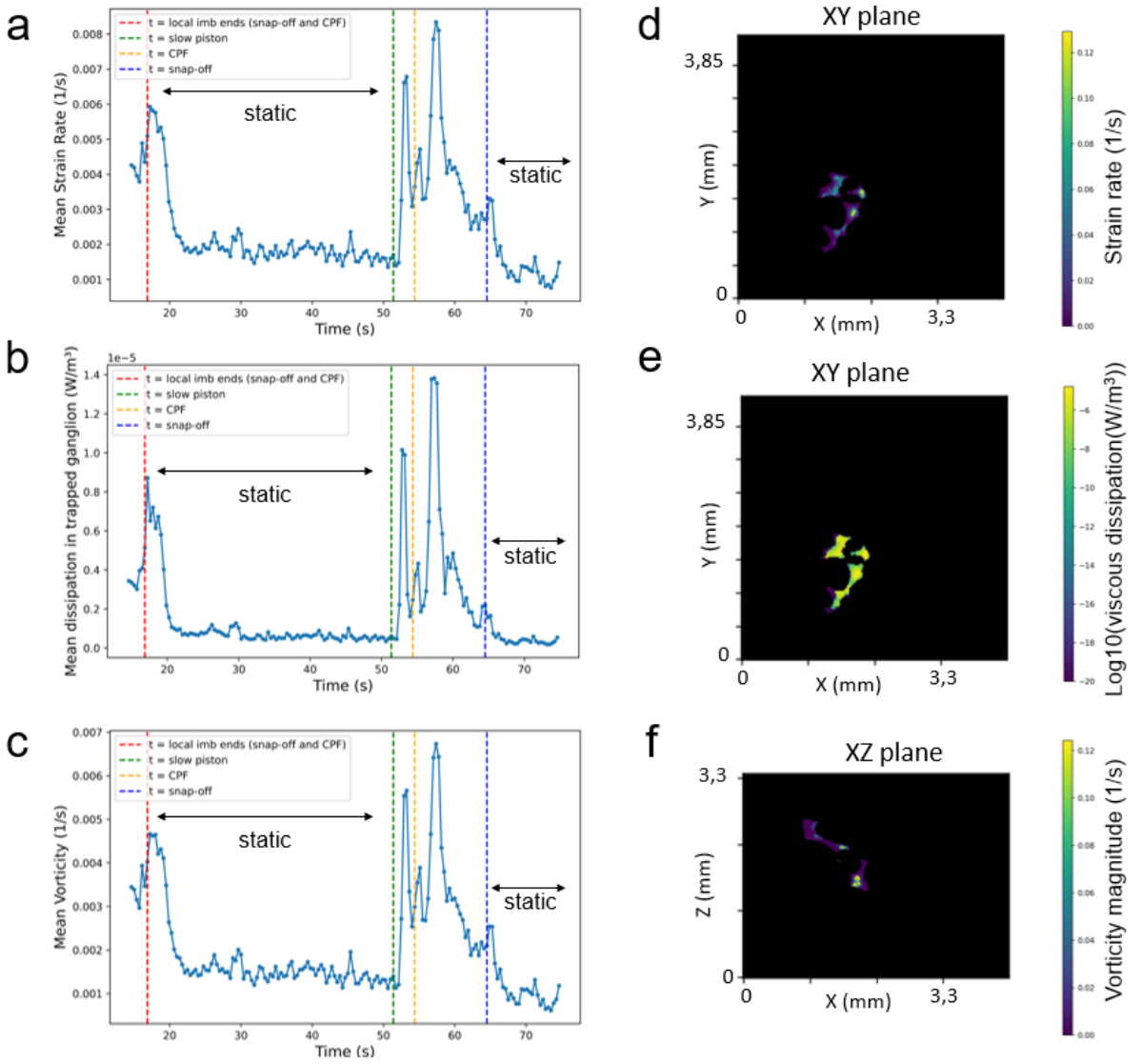


Figure S 6: a) mean strain rate within the trapped ganglion throughout the experiment. b) mean dissipation within the trapped ganglion throughout the experiment. c) cross-section in the XY plane showing the local strain rate within the trapped ganglion at 22.5s. d) cross-section in the XZ plane showing the local vorticity magnitude within the trapped ganglion at 22.5s.

viii. References

Bultreys, T., Van Offenwert, S., Goethals, W., Boone, M. N., Aelterman, J., & Cnudde, V. (2022). X-ray tomographic micro-particle velocimetry in porous media. *Physics of Fluids*, 34(4), 042008. https://doi.org/10.1063/5.0088000

Kuhn, H. W. (1955). The Hungarian method for the assignment problem. *Naval Research Logistics Quarterly*, 2(1–2), 83–97. https://doi.org/10.1002/nav.3800020109

Zarikos, I., Terzis, A., Hassanizadeh, S. M., & Weigand, B. (2018). Velocity distributions in trapped and mobilized non-wetting phase ganglia in porous media. *Scientific Reports*, 8, 13228. https://doi.org/10.1038/s41598-018-31639-4